EUROPEAN ORGANIZATION FOR NUCLEAR RESEARCH

CERN-PPE / 92 - 36
January 20th. 1992.

Observation of the UV scintillation light from high energy electron showers in liquid Xenon.

A. Braem, A. Gonidec, D. Schinzel, W. Seidl.
CERN, Geneva, Switzerland.

E. F. Clayton, G. Davies, G. Hall, R. Payne, S. Roe, C. Seez, J. Striebig, T. S. Virdee.
Blackett Laboratory, Imperial College, London SW7 2BZ, UK.

D. J. A. Cockerill.
Rutherford Appleton Laboratory, Chilton, UK.

ABSTRACT

The UV scintillation light in liquid xenon has been observed using silicon drift photodiodes. Measurements were carried out in a rectangular light cell of dimensions 7.4 x 7.4 x 60 cm^3 using 5 GeV electrons. The photodiodes and the preamplifiers were immersed in the liquid. A high quantum efficiency for 175 nm UV light has been measured. The scintillation light yield is found to be $(1.5\pm0.6).10^4$ photons per MeV of energy deposited in liquid xenon. A light attenuation length of $\approx$ 40 cm has been measured.

1. Introduction

The use of liquefied noble gases, like xenon (LXe) and krypton (LKr), for high resolution (and also high speed) calorimetry has recently evoked a great deal of interest, especially in connection with future hadron colliders [1]. Noble liquids are believed to be able to withstand large radiation doses although the radiation hardness of a system will probably be limited by the hardness of the read-out elements. The deposited energy in such liquids can be measured either by the collection of the ionization electrons, by the collection of the UV scintillation light or both. Results on the energy resolution attained in large LXe and LKr calorimeters using the collection of charge generated by high energy electron showers have been reported [2]. The alternative of scintillation light detection offers the advantage of high speed operation since much of the light is emitted in a very short time interval after excitation of the liquid. Other advantages include insensitivity to magnetic fields and the need of only modest purity. There is also the possibility, not yet demonstrated, of obtaining e/h closer to 1 by exploiting the different scintillation decay constants for lightly and heavily ionizing particles and the absence of saturation of the scintillation light yield up to very high LET radiation.

The relevant properties of some noble liquids are listed in Table 1. Of the noble liquids, LXe has the shortest radiation length, the smallest scintillation decay time constant, the highest emission wavelength and the highest operating temperature. LXe is a scintillator with a light output which is ~20 times larger than that found in the fast component of BaF_2.

Light detection in the ultra-violet region presents some practical difficulties and the detector requires special attention. The major problem of the light collection method is the point to point non-uniformity of light collection. Individual calorimeter cells may have to be long, since the radiation length of LXe is fairly large, and narrow, as fine granularity is important. Most of the light will thus have to suffer several reflections. Surfaces of high reflectivity to 175 nm light are needed. Attenuation of light will also lead to non-uniformities which are undesirable and should be minimized as they lead to a sizeable systematic contribution to the energy resolution function. The main aim of the tests reported here was to address these issues.

In this paper we present results obtained from a liquid xenon filled cell of dimensions 7.4 x 7.4 x 60 cm^3. The scintillation light generated by high energy electron showers was detected by unconventional silicon drift photodiodes (SDPD). The experimental details are given in section 2. The results are considered in section 3 and conclusions are drawn in section 4.

2. Experimental Details

The experimental setup indicating the light collecting cell and the cryogenic system is shown in Fig.1. Below we describe the various components in detail.

2.1 Mechanical and Optical Properties of the Light Collecting Cell

The light collecting cell walls were made of 3 mm. thick plates of aluminium. The aluminium plates were held in place by three Teflon® rings. Boards carrying the preamplifiers and the UV light sensitive silicon drift photodiodes were mounted onto the two outermost teflon rings (Fig. 2a).

The preamplifiers were placed behind the photodiodes. This meant that the light sensitive volume started about 5 cm into the LXe volume. Hence a significant fraction of the shower energy (~25%) was deposited outside the light sensitive volume. The layout of the 1 x 1 cm^2 photodiodes at each end is shown in Fig. 2b.

The aluminium plates were lacquered to create a smooth surface. The plates were slowly retracted from a bath of lacquer [3] and baked in an oven at a temperature of 120 °C for 10 hours. The plates were made into mirrors by depositing a layer of 70 nm of pure aluminium. The aluminized surfaces were protected from oxidation by depositing 30 nm of $Mg F_2$. Both of these processes were carried out under vacuum. Further details of this procedure can be found in reference 4. The reflectivity of both faces of all the plates was measured using light at normal incidence. A typical measurement of reflectivity as a function of wavelength is shown in Fig 3. The reflectivity was measured to be greater than 85 % at 175 nm for all surfaces. The best surface of each plate was placed on the interior of the light cell.

2.2 The Si Drift Photodiodes and the Preamplifiers.

The silicon drift photodiodes (SDPD) are photodiodes based on the principle of the solid state drift chamber [5]. They were fabricated on n-type silicon with field shaping p-type electrodes diffused into the non-photosensitive surface to produce the drift field. The active area of 1 cm^2 was subdivided into five 2mm wide cells with a central n-type anode in each cell to collect the electron signal. The opposite face was constructed as a conventional photodiode, i.e. unmetallised to ensure good photosensitivity. The five cells of each diode were connected in parallel. The operating bias of the detectors was –90 V. Further details of the operation and performance are contained in reference 5.

The main advantage of these diodes is that they have a considerably lower capacitance than conventional silicon photodiodes, which gives them a potential for low noise readout, even with quite fast electronics. Due to the drift of electrons within the silicon a significant time is required to collect the signal fully. At room temperature this can be as much as 300 ns but as the drift velocity in silicon increases with decreasing temperature more rapid charge collection at lower temperature is achievable. A measurement of the drift time of such a diode as a function of energy deposit position transverse to the drift cells at a temperature of –91°C is shown in Fig 4.

In order to calculate the scintillation light yield the photosensitivity of the diodes as a function of wavelength is required. The external quantum efficiency (Q), defined as the number of electrons detected per incident photon, can be considered to be the product of three factors

$$Q = T \eta F ,$$

representing the transmittance (T) of photons into the diode, the internal quantum efficiency (η) and the collection efficiency (F) of the photo-ionized charge.

To evaluate the transmittance it is necessary to estimate the thickness of the oxide layer on the DSPD's. We measured the reflectivity at normal incidence using facilities at the UK National Physical Laboratory [6]. The reflectivity is modulated by interference effects depending upon the surface thickness and wavelength of incident light. Fig. 5 shows the transmittance (i.e. 1 - reflectivity) as a function of wavelength of incident light. The oxide layer was found to have a thickness of 233 nm. The transmittance as a function of the incident angle for light of wavelength 175 nm is shown in Fig.6. Refractive indices of 1.59 (see section 2.3) and 1.78 for LXe and silicon oxide respectively were used. It can be seen that at 175nm and normal incidence approximately 60% of the light is reflected.

The internal quantum efficiency is the number of electron hole-pairs generated per photon incident on bulk silicon assuming perfect transmission. This has been determined by others [7] and in the region of interest here the internal quantum yield is ~1.80.

The final factor, F, the charge collection efficiency, is the probability that a minority carrier generated at a certain distance from the surface will cross the junction before recombination. It is important to note that the absorption length for wavelengths below 300 nm is not a strong function of wavelength and is ~ 5 nm [8]. This guarantees that photoionization will occur but, to ensure observation of a signal, the carriers must migrate in an electric field or by diffusion to avoid recombination and thus signal loss. F may therefore depend on the operating conditions and construction of the diode; the diodes used in these tests were not constructed so as to maximise the UV response and improvements are known to be achievable. F can be determined from the measurements of the external quantum efficiency. The measurement of the quantum efficiency of three DSPD's is shown in Fig.7 [9]. A United Detector Technologies [10,11] UV sensitive Si photodiode, previously measured at the U.K. National Physical Laboratory, has been used to normalize the quantum efficiency. The systematic error on the absolute value of the quantum efficiency is quoted to be 25%. We observe no variation of quantum efficiency with operating bias ranging from –50 V to –150 V. These are d.c. observations. Charge collection times could be influenced by operating bias; for this reason the detectors should always be operated fully depleted which was the case in this test.

Since the factors η and F are not expected to depend on the angle of incidence the external quantum efficiency as a function of the angle can be estimated by correcting for reflectivity.

The readout electronics consisted of Laben 5254 charge sensitive preamplifiers followed by shaping amplifiers with adjustable gain and CR-$(RC)^2$ shaping with a peaking time of 0.6 μs. Although originally designed for room temperature operation, the preamplifiers were placed in the liquid. A linear decrease in gain was observed as the temperature was lowered. The gain at -110°C was ~75% of its value at room temperature.

An E.N.C. of ~ 1000 electrons was measured during the experimental run. At low temperature the leakage current contribution to the noise was negligible but no systematic increase in noise was observed as the equipment was brought to room temperature, suggesting that the preamplifier performance is degraded at low temperature. Power dissipation was not an important constraint here; the power consumption of the amplifier was 180 mW per channel.

It should be stressed that neither the diodes nor the electronics were optimized for these tests and full advantage was not taken of the speed of the diodes or the potential for power reduction. Rather, the emphasis was on demonstration of light detection using the diodes in an environment where our experience was limited.

2.3 The refractive index of liquid xenon

There is some uncertainty in the value of the refractive index of liquid xenon at a wavelength of 175 nm. We are not aware of any measurement of the refractive index of liquid xenon at this wavelength. Measurements of the refractive index over the wavelength range 350 - 650 nm are reported in reference 12. A modified form of the Lorentz-Lorenz equation gives a very good description of the data. Extrapolating down to a wavelength of 175 nm. gives a value of 1.59 for the refractive index (Fig. 8). The extrapolation is very sensitive to the functional form of the extrapolation and small changes in the value of the refractive index at the larger wavelengths.

2.4 The Cryogenic System and Temperature Control.

Xenon gas was produced by the Rare Gas Factory, Lisichansk, USSR and delivered to CERN in standard gas bottles. It was purified and liquefied into a special test cell which allowed the measurement of the free electron lifetime. The purifier consisted of an Oxisorb® followed by a filter containing a mixture of silica-gel and molecular sieves and finally a dust filter made of stainless steel with a pore-size of 0.5 μm. The gas passing through the filters was liquefied and frozen into a stainless steel container kept at liquid nitrogen temperature.

The storage container is heated and the evaporating gas is liquified into the cell to be used for a test. After the tests, the xenon gas is evaporated back into the storage container where it is kept frozen until further use. In this way xenon is kept clean and free of dust. Straight after purification the free electron lifetime in liquid xenon was measured to be ≥ 100 μs as can be seen from Fig. 9. Electron showers were measured in a drift gap of 1 cm at an applied voltage of 2.7 V. The observed pulse shape was compared with that expected for a given lifetime after convolution with the amplifier response function. The method used to determine the lifetime is described in reference 13.

The calorimeter cell was housed inside a stainless steel vessel, previously used for tests of a xenon sampling calorimeter for which about 8 litres of liquid xenon were

necessary. The stainless steel vessel was thermally insulated from the outer vessel by three teflon spacers at each end. The arrangement of inner vessel, vacuum vessel and cryostat are shown in Figure 1. Prior to filling the xenon detector the vacuum tank is evacuated using a diffusion pump backed by a rotary pump. The xenon detector itself is pumped, together with the transfer-line from the storage container, via the xenon filling line by a turbomolecular pump. This pump was switched off during the filling.

The cooling of the inner vessel was provided by two copper braids connecting the cryostat to the inner vessel (Fig.1) . A 20 μm thick layer of copper was deposited on the outside of the inner vessel to allow brazing of a 5 mm preshaped copper bar. A copper block containing a 40 W resistor is soldered in the centre of the copper bar. The copper block is connected via thick copper braids to the cryostat. Another copper braid is connected to a second copper block which is mounted on the neck of the filling tube. It is also equipped with a 40 W resistor. Both copper braids delivered a total cooling power of 150 W . In order to minimize radiation losses the detector vessel as well as the copper braids were surrounded by 25 layers of superinsulation. The liquid nitrogen in the cryostat had to be refilled every 12 hours. The cooling system proved to be very reliable and stable but insufficient for fast liquifaction. Therefore, an auxilliary cooling system, consisting of a liquid nitrogen coil brazed onto the 5 mm thick copper bar described above, was used during the liquefaction of xenon gas. The nitrogen flow was regulated such that the xenon pressure always stayed above the triple point. After liquefaction the auxilliary sytem was switched off and disconnected.

The temperature of liquid xenon can be deduced from the vapour pressure which was measured using a stainless steel membrane pressure transducer. The signal from the pressure transducer was amplified and fed into a comparator whose reference could be set externally. The output of the comparator was used to alter the current through the heating resistors R (Fig. 1). After some time the pressure, and hence the temperature, of liquid xenon stabilizes to the desired value with a stability of ±10 mbar which is equivalent to $\Delta T \approx \pm 0.15$ °K. The temperature and pressure at the triple point are 161.25 K and 0.806 bar. The pressure transducer had been previously calibrated using a high precision mechanical membrane transducer. The vapour pressure curve of liquid Xenon was reproduced to within 1 % in the region of interest, i.e. from the triple point to 1 bar.

2.5 The Beam

The CERN-PS T7 test beam, providing electrons with momenta up to 7 GeV/c, was used to test the prototype. The layout included beam-defining trigger scintillation counters, beam halo veto scintillator, two Cherenkov counters to select electrons, and a wire chamber to measure the position of the beam particles. All the tests described below were carried out with 5 GeV/c electrons.

2.6 Light Collection Monte Carlo

The operation of the test cell was simulated using a Monte Carlo program. This consisted of two main sections :

i) simulation of the shower development in the entire experimental apparatus, and in particular the deposition of energy within the sensitive volume of the cell, and

ii) simulation of the propagation of 175 nm light through the cell, including reflections from the sides, and its collection by the eight SDPD's.

The development of the showers in the test cell and in the materials surrounding it was done using the program GEANT [14]. The test cell itself was represented as a rectangular volume of LXe contained in an aluminium box, which was itself contained inside a stainless steel cylinder filled with LXe.

The GEANT-based program could follow the development of showers produced by particles incident either on the end of the test rig, or at any position along the side of the rig. The parameters of the beam, such as its spread in energy or position, could be adjusted to agree with those measured during the tests.

As each Monte Carlo shower developed, the energy deposited inside the sensitive volume of the cell was accumulated and stored. In order to preserve the spatial distribution of this deposition, the cell was divided into cubes with a side of 1 cm. The total energy deposited in each of the 2940 cubes of LXe was written out to a file when the development of the shower terminated. After the generation of many events (typically 5000) this file constituted a 'library' of showers which could be used in the final stage of the Monte Carlo simulation.

The propagation of scintillation light, and its collection by the photo-diodes was simulated using a ray-tracing technique. Taking the centre of each of the cubes defined in the GEANT Monte Carlo as a source position, a large number of light-rays (usually 100,000) was generated, with a uniform spatial distribution, and each light-ray was traced until it struck one end of the cell. If the light-ray did not intersect the end at a position occupied by the sensitive area of one of the diodes, it was regarded as 'lost' (i.e. the material surrounding the diodes was assumed to be a perfect absorber for 175 nm light). Otherwise a decision was made as to whether the light-ray would be detected (absorbed) by the diode or reflected back into the LXe. This decision was based on the value of the transmission coefficient for the incident angle of interest using the functional form shown in Fig. 6.

At each reflection from a side-wall of the cell the light-ray was given a weight to account for the probability that it would be reflected. This probability was a function of the angle of incidence and took account of the reflection properties of the aluminized surface of the cell walls and their thin coating of Mg F_2. Its form is shown in Fig. 10. The value at normal incidence is taken from Fig. 2.

The finite attenuation length of the LXe was taken into account by applying an exponential weighting factor to each light-ray 'detected' by a diode. This factor depended on the value assumed for λ_{att}, the attenuation length in LXe, and on L_{tot}, the total length of

the light ray. The ratio of the summed weights of all light-rays 'detected' by a diode to the total number of light rays emitted at a given source position gave the efficiency of that diode for the detection of scintillation light emitted at that source position. The output from this section of the Monte Carlo therefore consisited of a large matrix containing the calculated light-collection efficiencies of each of the diodes for each of the 2940 possible source positions within the LXe volume.

The final predictions were produced by combining the results of the two sections in the following way. For each of the showers in the library, the number of photons emitted at the position of the centre of the cubes was taken to be proportional to the energy deposited in each of the cubes. This was then weighted by the 8 values of light collection efficiency computed for the appropriate source position, to provide numbers which would be proportional to the response of each of the 8 diodes. The sum of these numbers, over all 2940 cubes, then gave the predicted diode signals for that shower.

By separating the generation of the showers from the calculation of the light collection efficiency, it was possible to investigate the effects of different attenuation lengths and of different reflection and transmission coefficients without going through the lengthy GEANT shower generation procedure each time. Conversely, it was possible to use the same light collection efficiency computations with different shower libraries, corresponding for example to different entry positions for the beam, or to different beam energies, without having to repeat the light collection efficiency calculations.

3. Results and Analysis.

3.1 Light Yield

The total signal observed by the eight diodes is shown in Fig. 11. A beam of 5 GeV electrons was incident perpendicular to one of the small faces as indicated in Fig. 1. Ten thousand events were recorded for offline analysis. A tail on the high side of the peak was observed. It was found to be due to events in which there was an anomalously large signal in one of the eight diodes. This tail was effectively removed by placing a cut ($\pm 4\ \sigma$) on the distributions $f_i / \Sigma f_i (i=1,4)$ where f_i is the signal seen by one of the four diodes on the front or the rear face. The effect is probably caused by an energy deposit directly in front of one of the diodes. Monte Carlo simulation shows that the light collection efficiency directly in front of a diode, increases by an order of magnitude compared with that for light generated close to diode plane but not in front of any of the four diodes. We believe that a beam halo may be responsible as the tail is almost fully removed when the cut is made on the front diodes only.

The number of photons, n_γ, emitted per unit energy deposited in LXe can be expressed as

$$n_\gamma = \frac{n_e}{E\ f_E\ f_l\ \eta\ F}$$

where

E is the incident particle energy in MeV

n_e is the observed number of photoelectrons,

f_E is the fraction of the shower energy deposited in the light sensitive volume,

f_ℓ is the fraction of the emitted light that is absorbed by SDPD's.

The mean number of photoelectrons observed is found to be $3.2\ 10^5$.

Monte Carlo simulation has been used to estimate $f_E=0.77\pm0.05$ and $f_\ell=(5.8\pm1.0).10^{-3}$. The value of ηF is deduced from the measurement of the transmittance of light at normal incidence (Figs. 5 and 6) and the external quantum efficiency (Fig. 7). T enters into the estimation of f_ℓ and thus a measurement of the external quantum efficiency is sufficient to obtain η F. Weighted by the emission spectrum of the scintillation light, the transmittance is estimated to be $\sim 45 \pm 5$ %. The external quantum efficiency is taken to be ~ 0.5 leading to $\eta F \sim 0.89$. The error in the value of the quantum efficiency, including the systematic error mentioned in section 2.2, is taken to be 0.15. The error in the calibration of the preamplifiers is estimated to be ~ 20%.

Using the above figures we find that $n_\gamma = (1.5 \pm 0.6).10^4$ photons / MeV. This is consistent with previous determinations [15,16] of the light yield giving $\approx 2.6.10^4$ photons / MeV.

3.2 Attenuation Length

The apparatus was rotated about the vertical by 90° and 5 GeV electrons were fired perpendicularly into the long sides as indicated by the insert in Fig. 13. The apparatus, placed on a mobile platform, was moved horizontally in steps of 5 cm. One thousand events were recorded for each position. The signal observed by the left and the right-hand side diodes is plotted in Fig. 12. The large difference in the observed signal close to, and far away, from the diode planes is mainly due to two effects, namely non-uniformity of light collection and attenuation of light. We introduced into the Monte Carlo our estimation of the reflectivity of the side walls as a function of the angle of incidence and the transmittance of light into the DSPD's as a function of incident angle. All the diodes were assumed to have the same quantum efficiency. Simulation was carried out for various values of the attenuation length of light in liquid xenon and the response of the left and right hand side diodes was estimated for different entry positions. Fig 13 shows observed and estimated ratio of responses from the two sides (normalized to the side with the lower response) as a function of the entry position of the beam. A satisfactory description of the data is obtained for an attenuation length of 40 cm.

An independent check of the attenuation length can be obtained by comparing the ratio of the observed signals in the front and rear diodes for the run with 5 GeV electrons where the electrons were incident normal to the plane of the diodes. The predicted value of the ratio is plotted as a function of attenuation length in Fig. 14a. The vertical bars represent the r.m.s. of the simulated distribution and not the error on the mean value. An attenuation length of $\approx$ 40 cm is favoured. Fig. 14b shows that the data are rather sensitive to the value

of the attenuation length and only the simulation using an attenuation length in the region of 40 cm reproduces both the shape and the mean value of the distribution of this ratio. Comparison with other measurements of the attenuation length in liquid xenon are difficult because of the scarcity of data. An attenuation length larger than 10 cm is reported in reference 17. It is not known if our value of the attenuation length is influenced by contamination of the liquid or is mainly due to the intrinsic properties of the liquid. It has to be stressed that no special cleaning of the components or bakeout procedures were followed before filling the sensitive volume with LXe.

3.3 Energy Resolution

Even with the beam incident along the longitudinal axis (Fig. 1a) a substantial fraction of the shower energy is deposited outside the light sensitive volume. Nevertheless we have attempted to understand the observed energy resolution in terms of the parameters described and discussed above. The values obtained from the simulation for σ/E are :

3.0 % due to energy leakage alone,

8.0 % after inclusion of light collection.

The values given are extracted from Gaussian fits to the distributions. This should be compared with the experimentally observed resolution of $\sigma/E = 9.5$ %. There is a reasonable agreement between the observed and the predicted resolutions. The role of the non-uniformity of light collection in worsening the resolution is clearly evident.

The intrinsic energy resolution in liquid xenon is expected to be much better. To date the best measurement of the energy resolution, using Si photodiodes as photosensors, gives an rms of 0.5 % for an energy deposit of 2.5 GeV from 92 MeV/n Al ions [18].

4. Conclusions

We have observed the UV scintillation light from high energy electron showers in more than 3 litres of liquid xenon. The light was observed by silicon drift photodiodes. This is the first time that these novel devices have been used as practical light detectors. The diodes and the associated preamplifiers were immersed in the liquid and performed well. The diodes were shown to have a high quantum efficiency for UV light. The amount of scintillation light per unit energy deposit in LXe is found to be $(1.5 \pm 0.6)\ 10^4$ photons per MeV of deposited energy, and is consistent with previous measurements. The data favour a light attenuation length in liquid xenon of around 40 cm at a wavelength of 175 nm. These results indicate that a practical electromagnetic calorimeter based on the detection of the scintillation light by Si photodiodes immersed in liquid xenon is feasible.

Acknowledgements

Several useful discussions with M. Chen and T. Ypsilantis are gratefully acknowledged. We also acknowledge the help of L. Toudup and the electrical and mechanical workshops at Imperial College, and P. Dreesen, C. David, D. Carminati at CERN.

References

[1] M. Chen et al., Nucl. Instr. and Meth., A267 (1988) 43.
J. Seguinot et al., CERN-LAA/89-1 (1989), CERN-LAA/PC/90-24 (1990).
E. Clayton et al., IC/HEP/90-9 (1990), Blackett Lab., Imperial College, London.
[2] V.M.Aulchenko et al., Nucl. Instr. and Meths., A289 (1990) 468.
A. Baranov et al., CERN EP/90-03, 1990.
[3] S700 Thermosetting Acrylic Lacquer, Neogene Paints, London W2 5HQ. UK.
[4] P. Baillon et al., Nucl. Instr. and Meth. A277 (1989) 338.
[5] B.S. Avset et al., Nucl. Instr. and Meth. A288 (1990) 131.
[6] S. Roe, preprint IC/HEP/91-3 (1991), Blackett Lab., Imperial College, U.K.
[7] J. Geist, Phys. Rev. B27 (1983) 8.
[8] Properties of Silicon, EMIS Data Review, INSPEC publication, London, 1986.
[9] G. Davies et al., Preprint IC/HEP/91-9 (1991), Blackett Lab, Imperial College, U.K.
[10] UDT, 12525 Chadon Avenue, Hawthorne, CA, USA.
[11] L.R. Canfield et al., Applied Optics 28 (1989) 3940.
[12] A.C. Sinnock and B.L. Smith, Phys. Rev. 181 (1969) 1297.
[13] M. Albrow et al., Nucl. Instr. and Meths., A305 (1991) 331.
[14] GEANT 3.14, Users's Manual DD/EE/84-1 (1984), CERN Data Handling Division.
[15] E. Aprile et al., Proc. of IEEE 1989 Nuclear Science Symposium (1990), San Fransisco, U.S.A. 1990.
[16] J. Seguinot et al., CERN/AT-CR/91-08, 1991.
[17] T. Ypsilantis, CERN 90-10, Proceedings of ECFA LHC Workshop, Aachen (1990).
[18] K. Masuda et al., Nucl. Instr. and Meths. A309 (1991) 489.

Figure Captions

Fig. 1 The experimental layout.
Fig. 2 a) The layout of the preampliers and b) of the photodiodes.
Fig. 3 The reflectivity of the aluminized cell walls versus wavelength for perpendicular incidence in vacuo.
Fig. 4 Measurements of the drift time as a function of position transverse to the drift cells for two temperatures.
Fig. 5 Transmittance (1 – reflectance) versus wavelength for a photodiode in vacuo.
Fig. 6 Transmittance versus angle of incidence for 175 nm light in a photodiode immersed in liquid xenon. Estimates for two refractive indices of liquid xenon are shown.
Fig. 7 Measurement of the external quantum efficiency as a function of wavelength for three photodiodes.
Fig. 8 Extrapolation of the refractive index of liquid xenon as a function of wavelength from measurements above 350 nm.
Fig. 9 The time evolution of the observed ionization charge in liquid xenon for a gap of 1 cm and a field of 2.7 V.
Fig. 10 The reflectance of the aluminized side-walls as a function of the angle of incidence for 175 nm light in liquid xenon.
Fig. 11 The observed signal for 5 GeV electron showers.
Fig. 12 The signal observed by the l.h.s. (•) and r.h.s. (o) SDPD's when the beam is fired perpendicular to the long sides of the rectangular cell.
Fig. 13 The observed and estimated (for different light attenuation lengths) ratio of the responses from the l.h.s. and r.h.s. SDPD's, normalized to the side with the lower response, as a function of the entry position of the beam.
Fig. 14 a) The ratio of the observed signal in the front and rear SDPD's is compared with that estimated for different attenuation lengths (open squares). The vertical bars represent the r.m.s. of the simulated ratio distribution.
b) Comparison of the ratio distribution for data and simulation (histogram).

Table 1. Properties of noble liquids.

		LAr	LKr	LXe
Density	g/cm^3	1.39	2.45	3.06
dE/dx <mip>	MeV / cm	2.11	3.45	3.89
Radiation Length	cm	14.3	4.76	2.77
Moliere Radius*	cm	7.3	4.7	4.1
Photons/MeV [16]	k		19	26
% light in fast component		8	1	77
Decay Const. Fast	ns	6.5	2	2
Slow	ns	1100	85	30
λ peak	nm	130	150	175
Refractive Index @ 170nm		-	1.41	1.60
Drift vel (10kV/cm)	cm/μs	0.5	0.5	0.3
Fano Factor		0.11	0.06	0.05
Dielectric Constant		1.51	1.66	1.95
Triple Point Temperature	K	84	116	161
Pressure	bar	0.67	0.72	0.80

* PDG definition

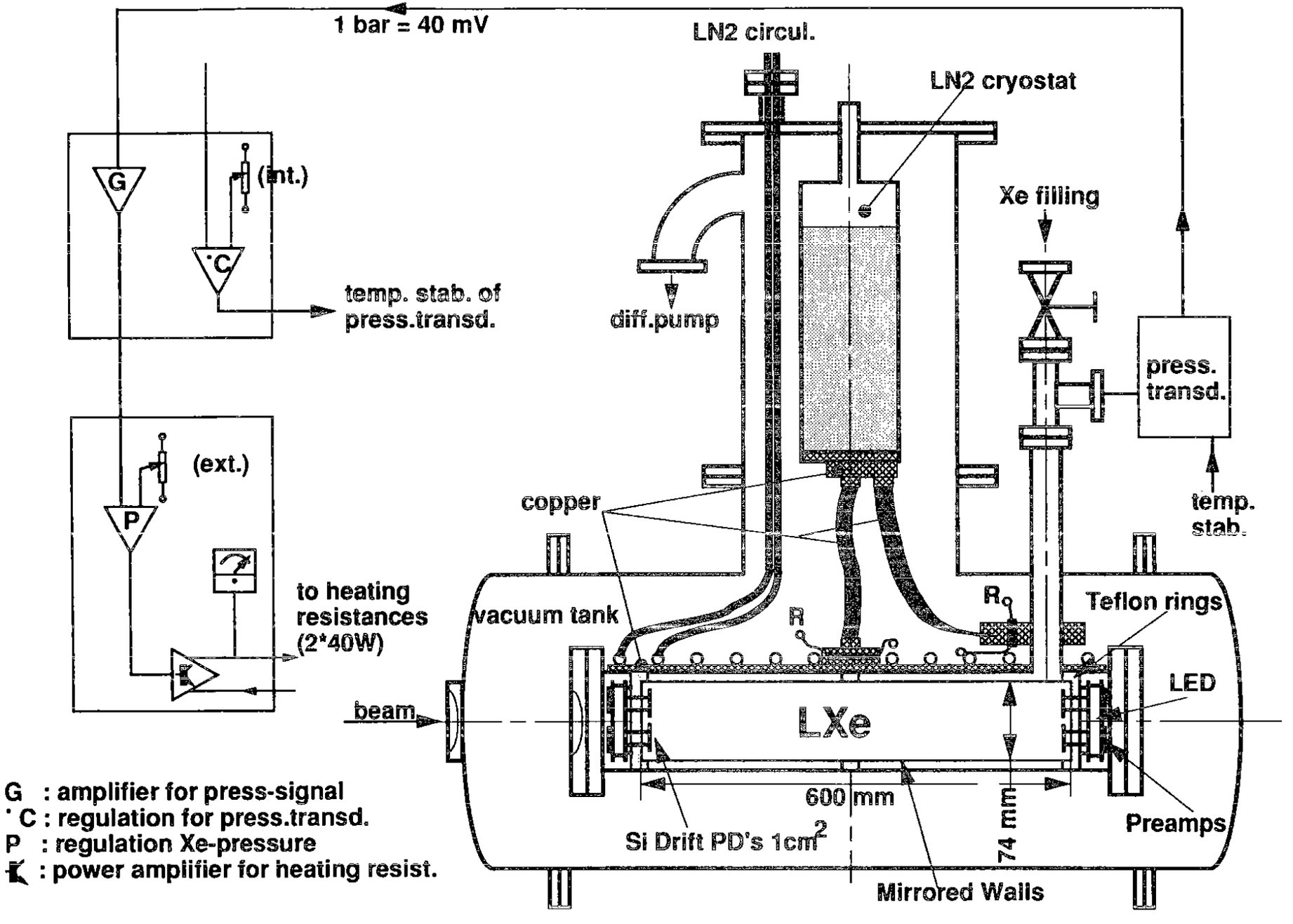
1 bar = 40 mV
LN2 circul.
LN2 cryostat
G
(int.)
°C
temp. stab. of
press.transd.
diff.pump
Xe filling
press.
transd.
temp.
stab.
(ext.)
P
copper
to heating
resistances
(2*40W)
vacuum tank
R
R
Teflon rings
LED
beam
LXe
600 mm
74 mm
Si Drift PD's 1cm²
Preamps
Mirrored Walls
G : amplifier for press-signal
° C : regulation for press.transd.
P : regulation Xe-pressure
: power amplifier for heating resist.

Fig. 1

(a)

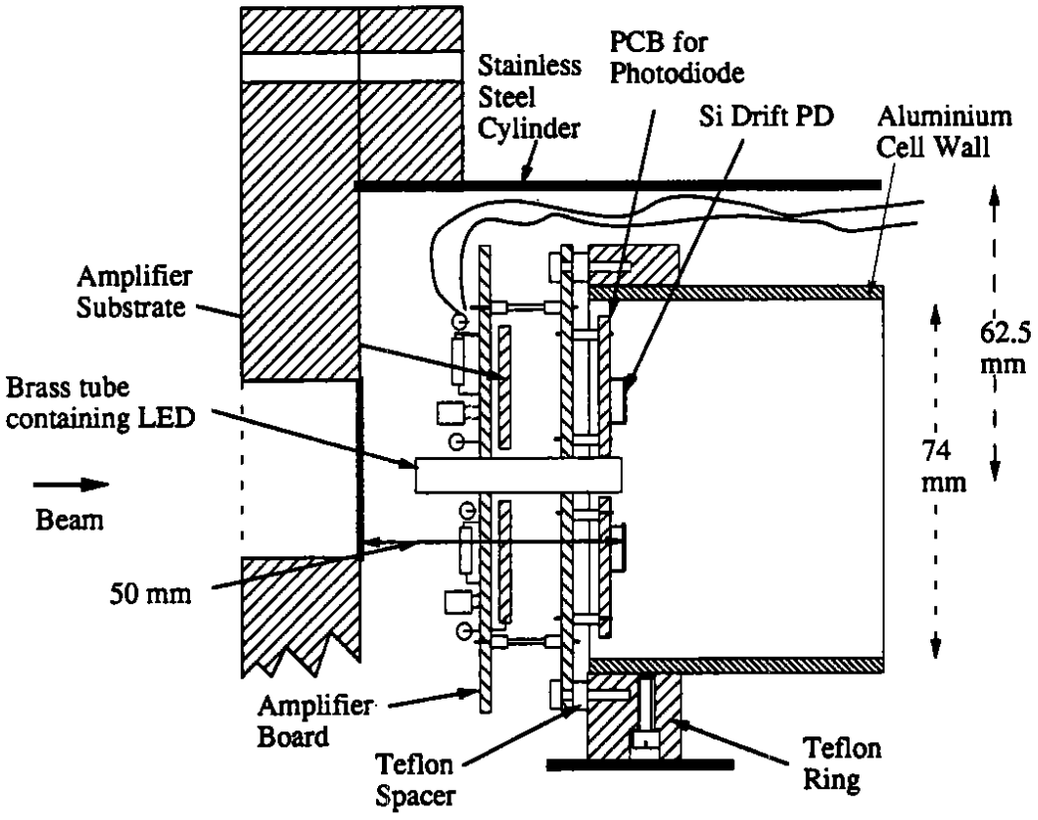
Stainless Steel Cylinder
PCB for Photodiode
Si Drift PD
Aluminium Cell Wall
Amplifier Substrate
Brass tube containing LED
Beam
50 mm
62.5 mm
74 mm
Amplifier Board
Teflon Spacer
Teflon Ring

Fig. 2

(b)

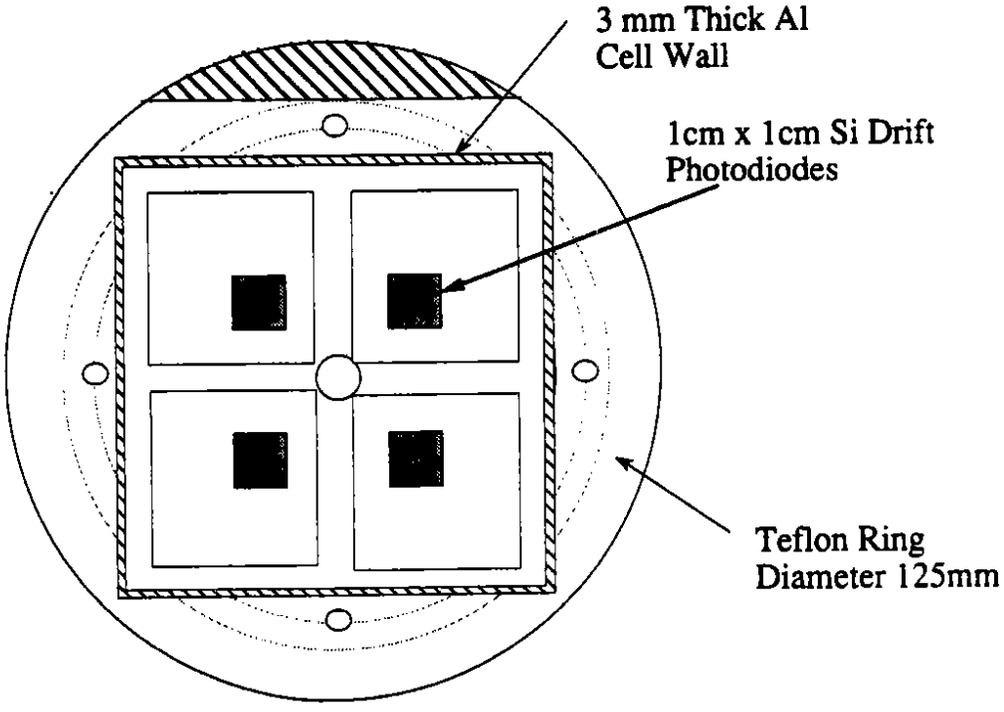
3 mm Thick Al Cell Wall
1cm x 1cm Si Drift Photodiodes
Teflon Ring Diameter 125mm

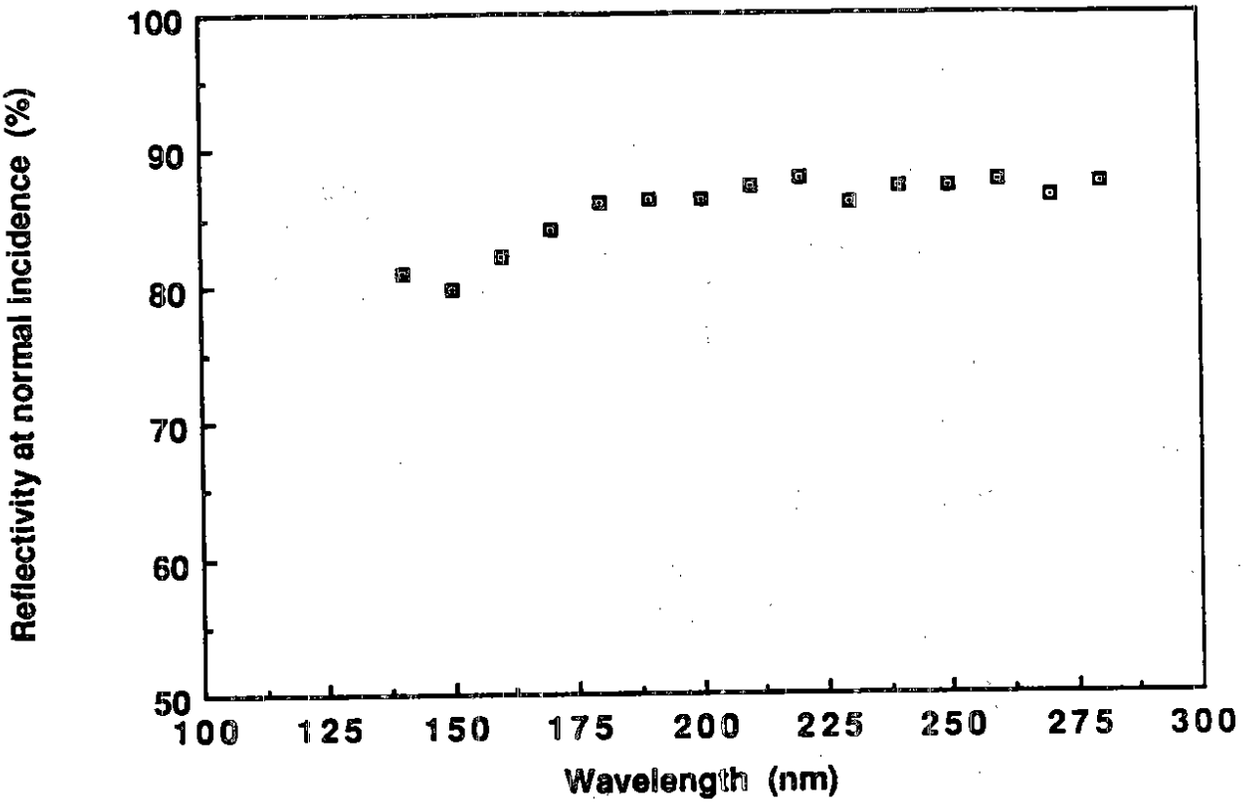
Reflectivity at normal incidence (%)
100
90
80
70
60
50
100
125
150
175
200
225
250
275
300
Wavelength (nm)

Fig. 3

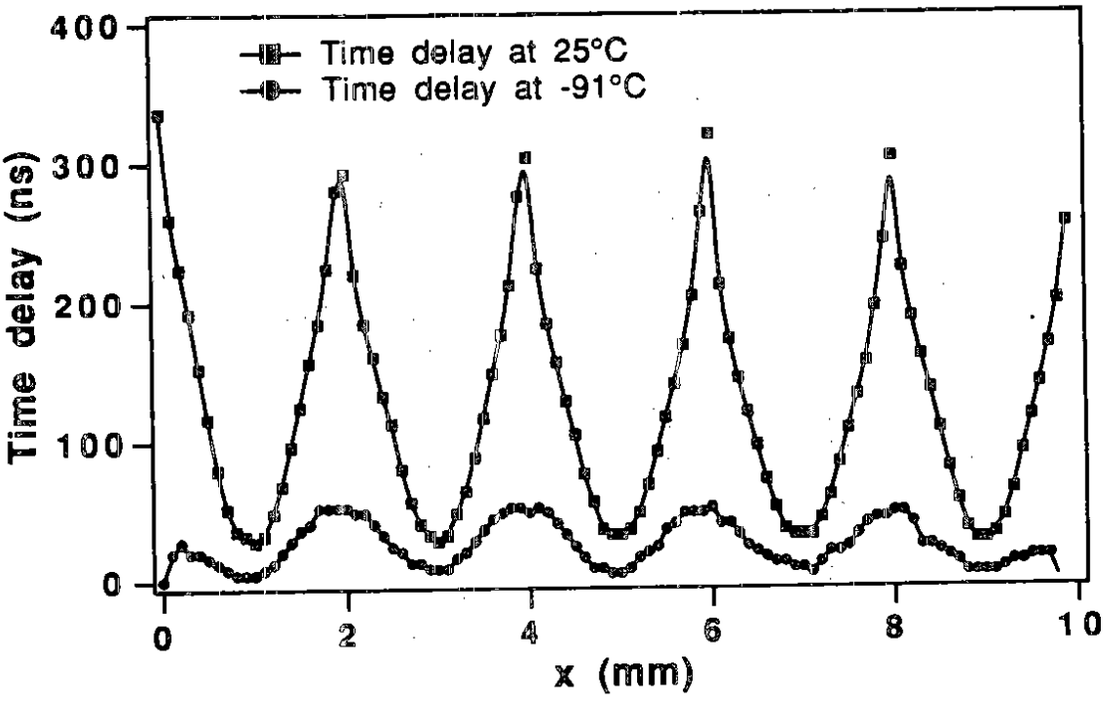
Time delay at 25°C
Time delay at -91°C
Time delay (ns)
400
300
200
100
0
0
2
4
6
8
10
x (mm)

Fig. 4

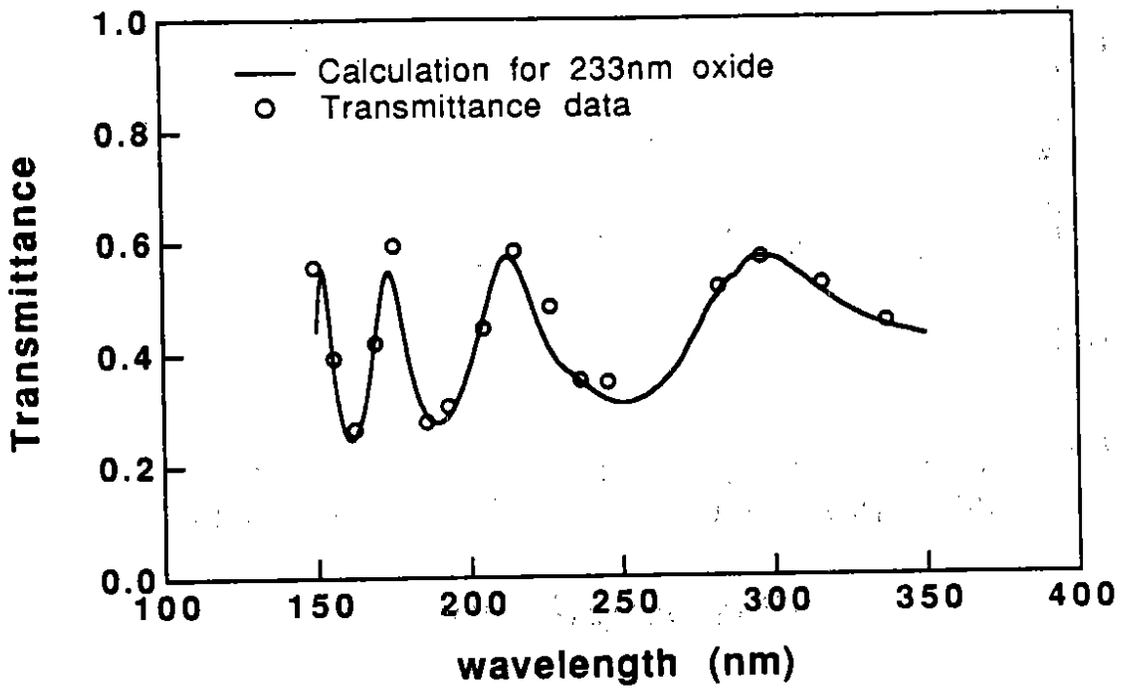
Calculation for 233nm oxide
Transmittance data
Transmittance
1.0
0.8
0.6
0.4
0.2
0.0
100
150
200
250
300
350
400
wavelength (nm)

Fig. 5

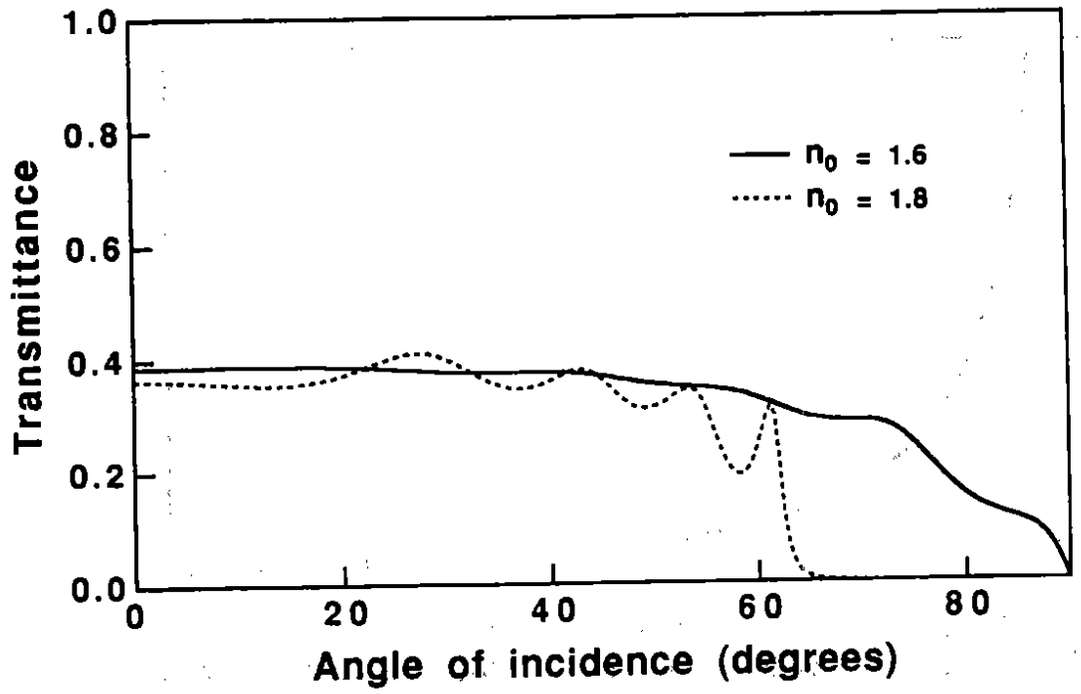
n_0 = 1.6
n_0 = 1.8
Transmittance
1.0
0.8
0.6
0.4
0.2
0.0
0
20
40
60
80
Angle of incidence (degrees)

Fig. 6

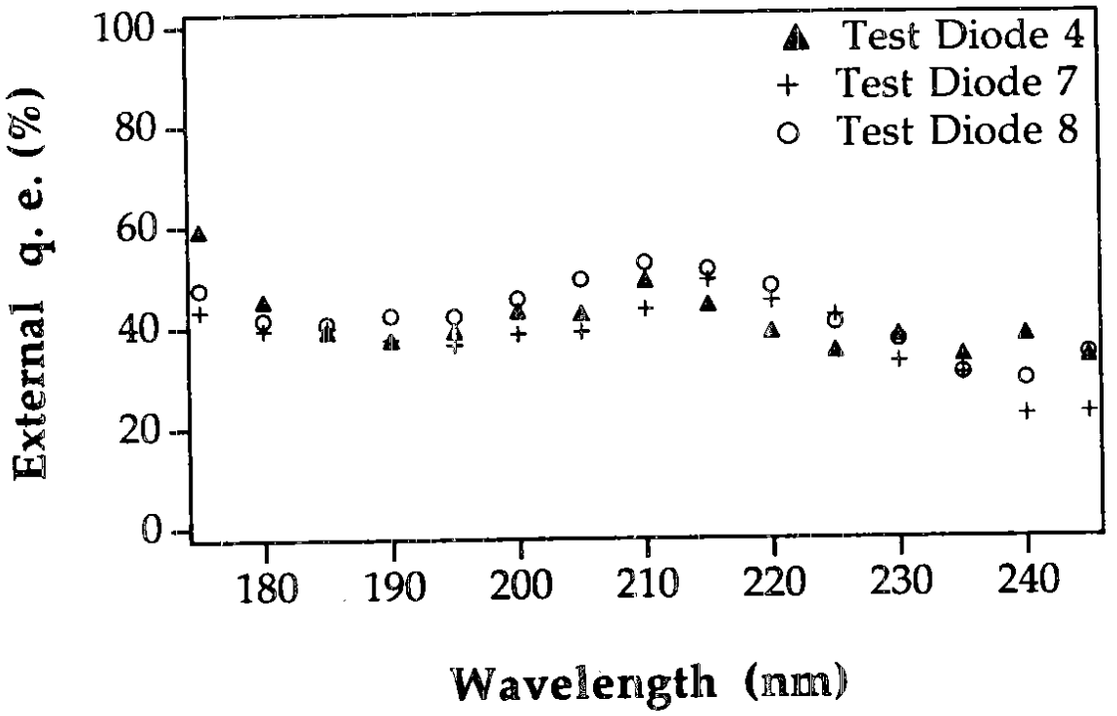
External q. e. (%)
100
80
60
40
20
0
180
190
200
210
220
230
240
Test Diode 4
Test Diode 7
Test Diode 8
Wavelength (nm)

Fig. 7

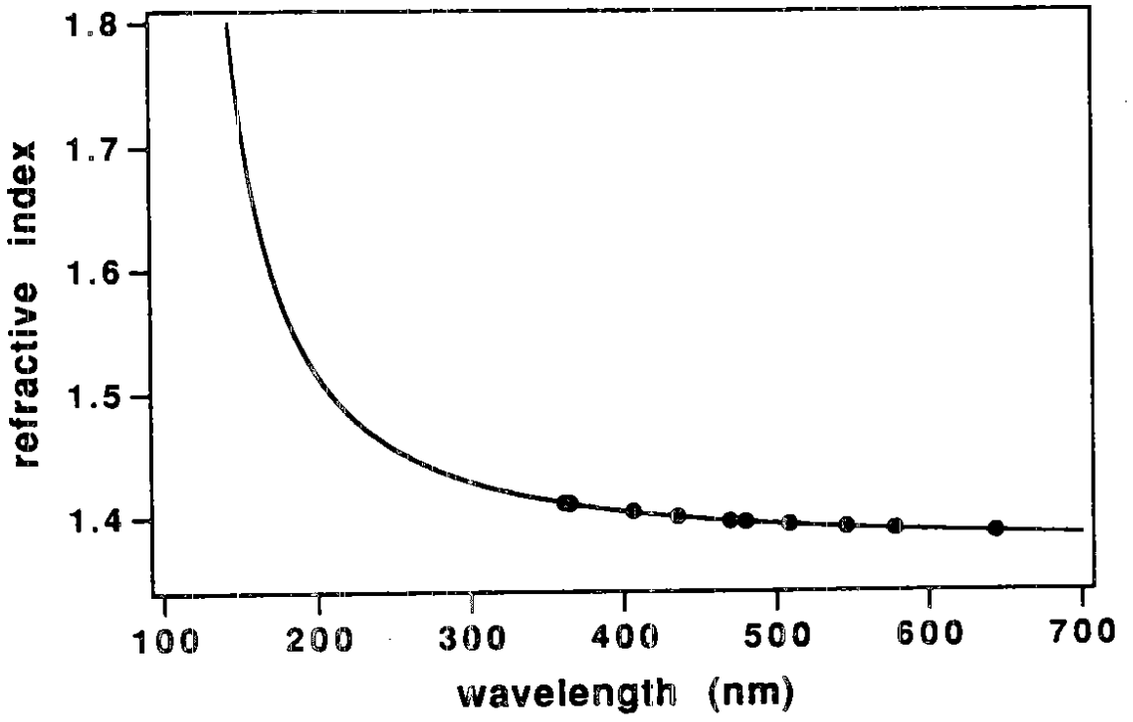
refractive index
1.8
1.7
1.6
1.5
1.4
100
200
300
400
500
600
700
wavelength (nm)

Fig. 8

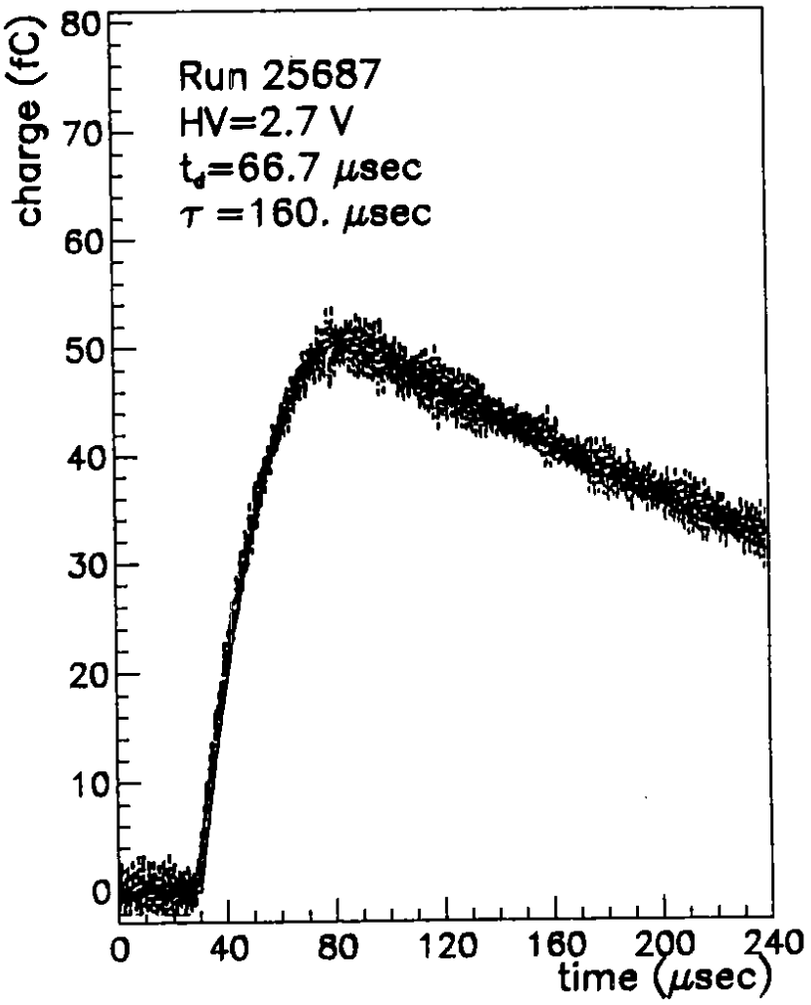
Run 25687
HV=2.7 V
t_d=66.7 μsec
τ =160. μsec
charge (fC)
time (μsec)
0
10
20
30
40
50
60
70
80
0
40
80
120
160
200
240

Fig. 9

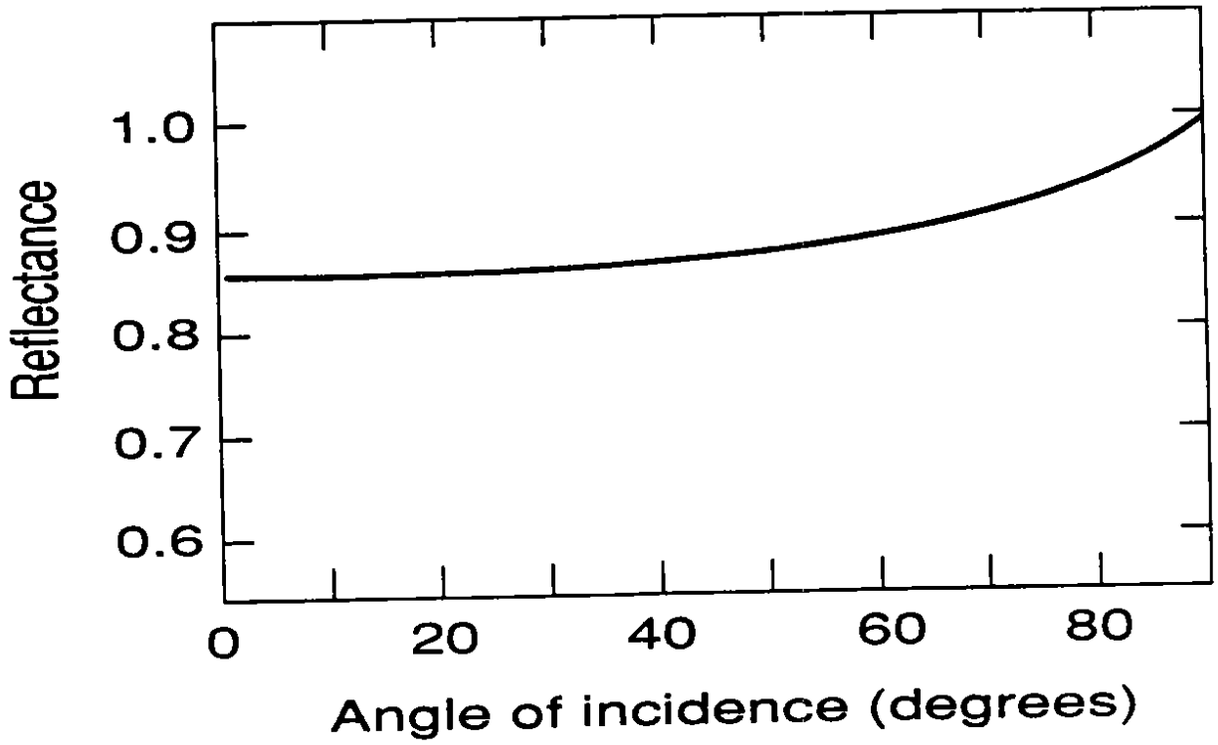
Reflectance
Angle of incidence (degrees)
0.6
0.7
0.8
0.9
1.0
0
20
40
60
80

Fig. 10

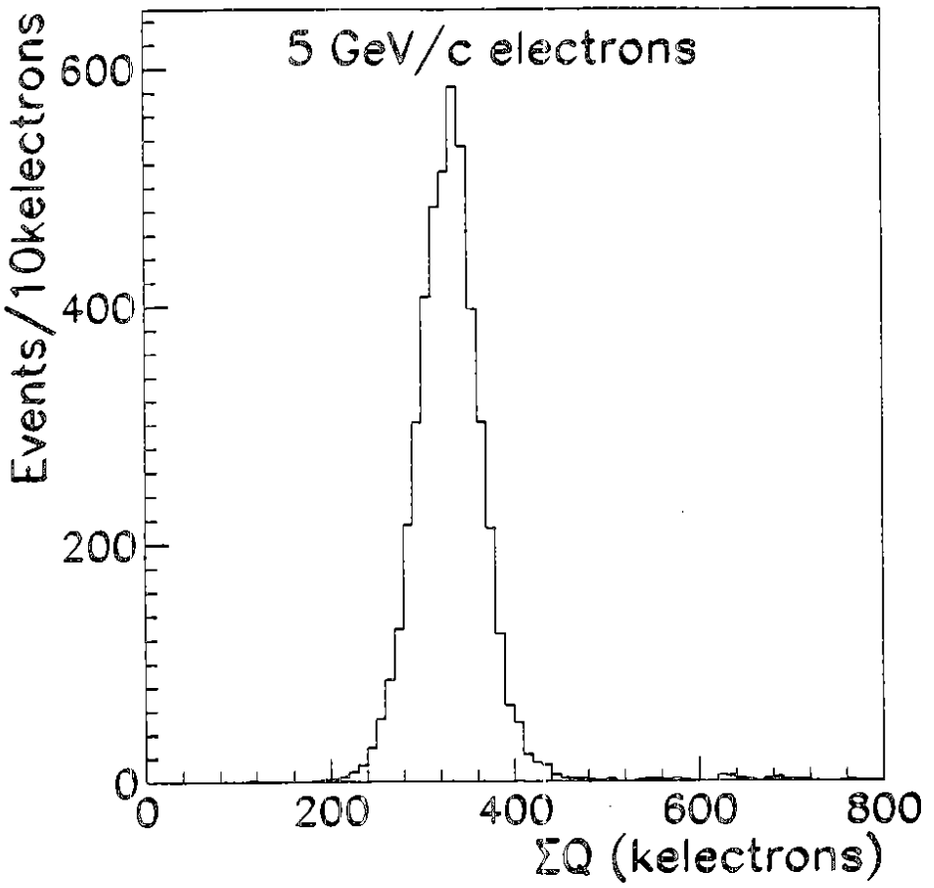
5 GeV/c electrons
Events/10kelectrons
600
400
200
0
0
200
400
600
800
ΣQ (kelectrons)

Fig. 11

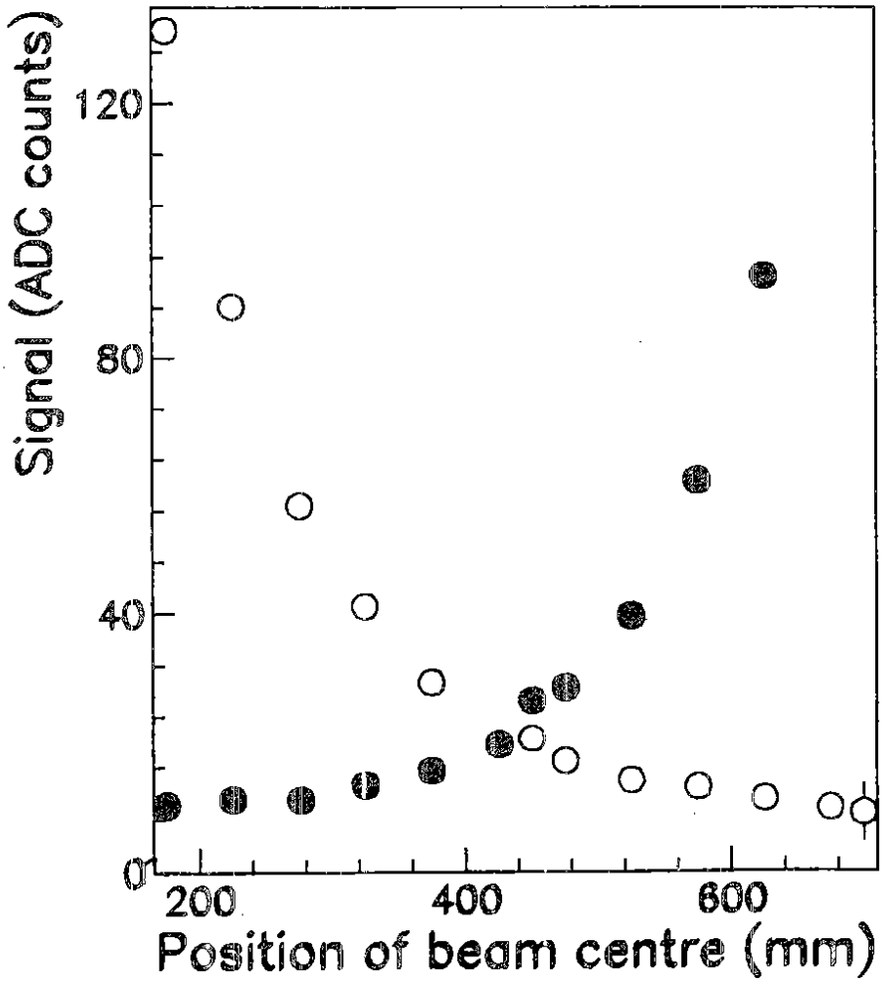
Signal (ADC counts)
120
80
40
0
200
400
600
Position of beam centre (mm)

Fig. 12

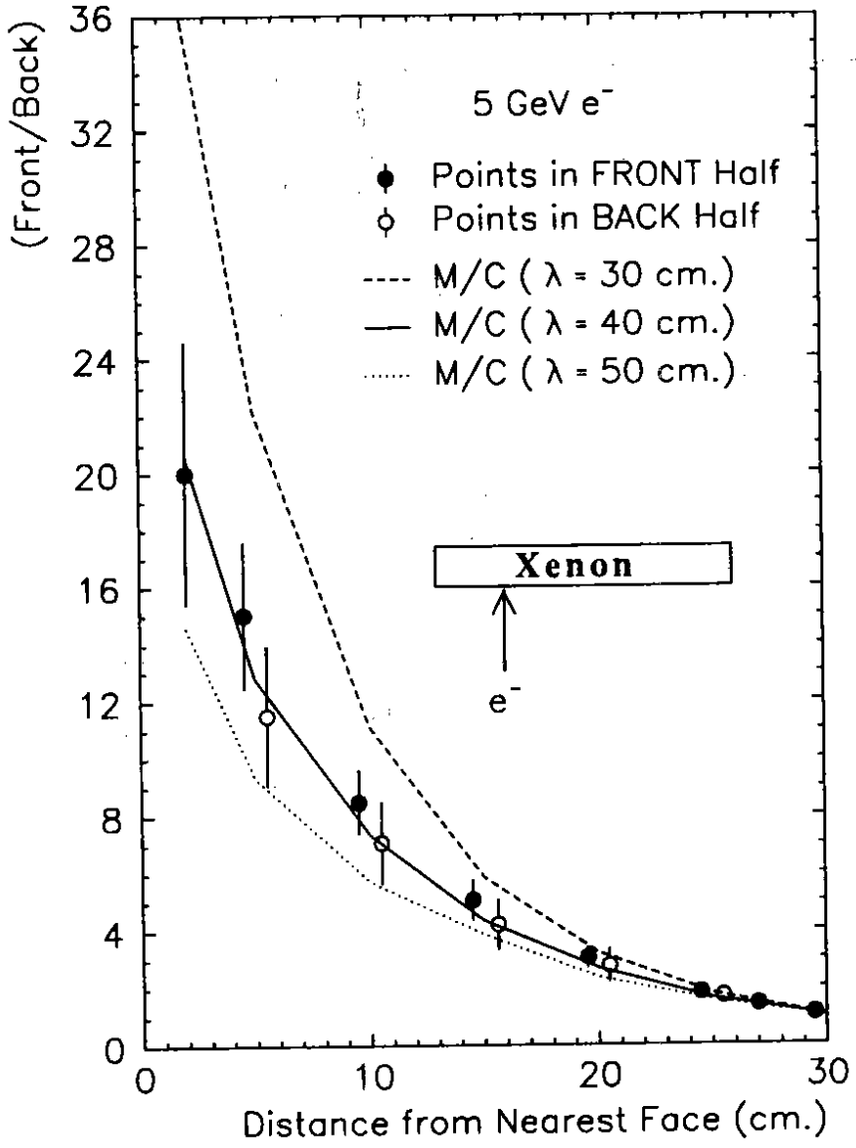
(Front/Back)
36
32
28
24
20
16
12
8
4
0
0
10
20
30
Distance from Nearest Face (cm.)
5 GeV e⁻
Points in FRONT Half
Points in BACK Half
M/C (λ = 30 cm.)
M/C (λ = 40 cm.)
M/C (λ = 50 cm.)
Xenon
e⁻

Fig. 13

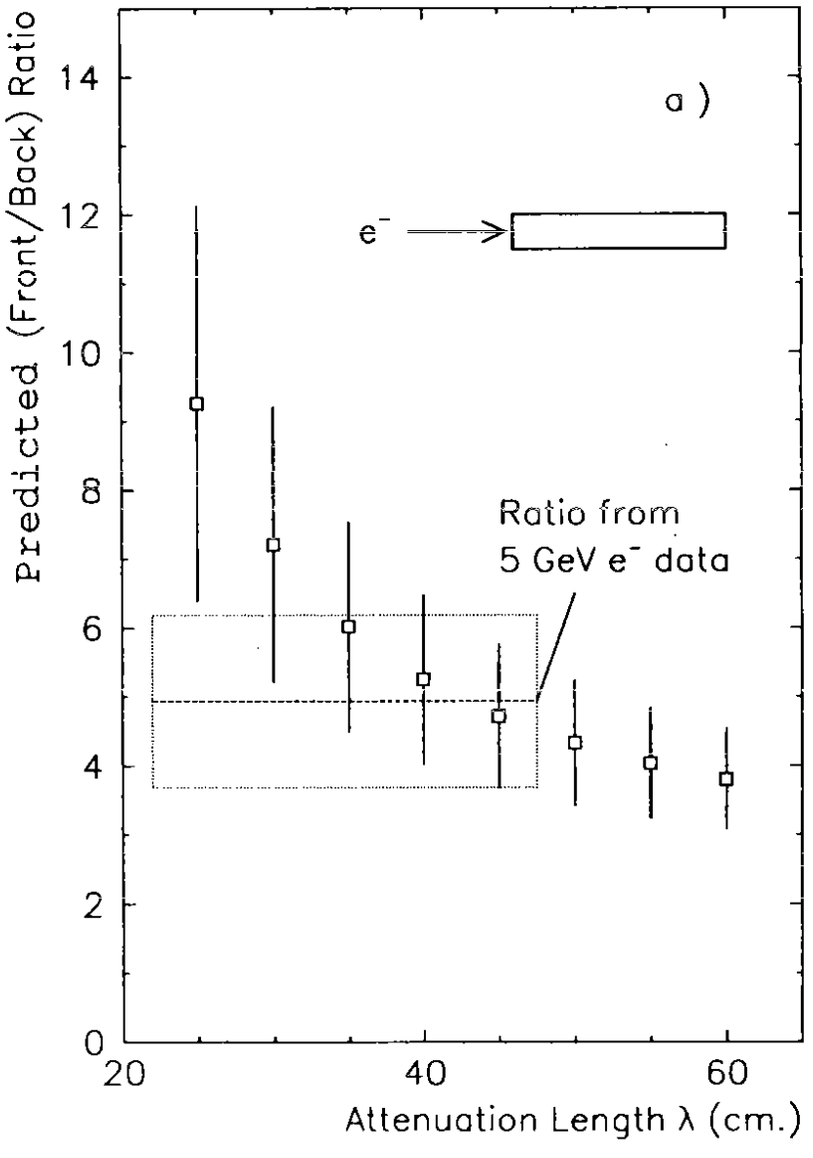
a)
e⁻
Ratio from
5 GeV e⁻ data
Predicted (Front/Back) Ratio
Attenuation Length λ (cm.)
0
2
4
6
8
10
12
14
20
40
60

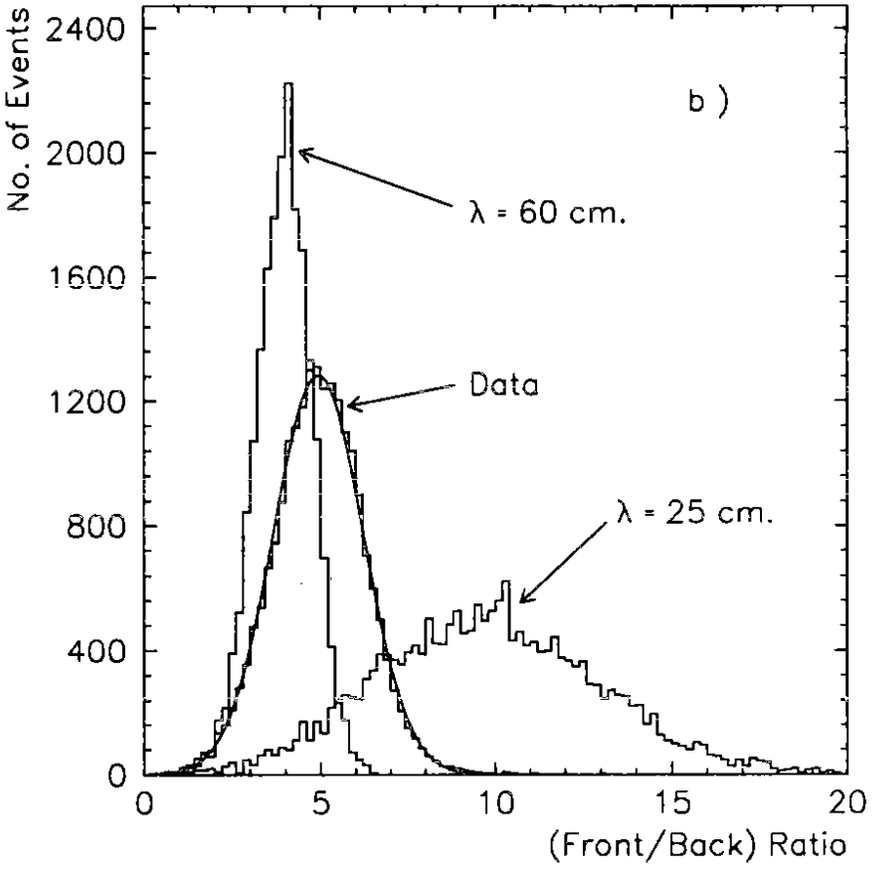
b)
λ = 60 cm.
Data
λ = 25 cm.
No. of Events
(Front/Back) Ratio
0
400
800
1200
1600
2000
2400
0
5
10
15
20

Fig. 14